

Rare-Earth Metal(III) Oxide Selenides $M_4O_4Se[Se_2]$ ($M = La, Ce, Pr, Nd, Sm$) with Discrete Diselenide Units: Crystal Structures, Magnetic Frustration, and Other Properties

Sabine Strobel,^{†,‡} Amitava Choudhury,[‡] Peter K. Dorhout,[‡] Christian Lipp,[†] and Thomas Schleid^{*†}

Institute for Inorganic Chemistry, Universitaet Stuttgart, Pfaffenwaldring 55, D-70569 Stuttgart, Germany, and Department of Chemistry, Colorado State University, Fort Collins, Colorado 80523

Received February 6, 2008

The rare-earth metal(III) oxide selenides of the formula $La_4O_4Se[Se_2]$, $Ce_4O_4Se[Se_2]$, $Pr_4O_4Se[Se_2]$, $Nd_4O_4Se[Se_2]$, and $Sm_4O_4Se[Se_2]$ were synthesized from a mixture of the elements with selenium dioxide as the oxygen source at 750 °C. Single crystal X-ray diffraction was used to determine their crystal structures. The isostructural compounds $M_4O_4Se[Se_2]$ ($M = La, Ce, Pr, Nd, Sm$) crystallize in the orthorhombic space group *Amm2* with cell dimensions $a = 857.94(7)$, $b = 409.44(4)$, $c = 1316.49(8)$ pm for $M = La$; $a = 851.37(6)$, $b = 404.82(3)$, $c = 1296.83(9)$ pm for $M = Ce$; $a = 849.92(6)$, $b = 402.78(3)$, $c = 1292.57(9)$ pm for $M = Pr$; $a = 845.68(4)$, $b = 398.83(2)$, $c = 1282.45(7)$ pm for $M = Nd$; and $a = 840.08(5)$, $b = 394.04(3)$, $c = 1263.83(6)$ pm for $M = Sm$ ($Z = 2$). In their crystal structures, Se^{2-} anions as well as $[Se-Se]^{2-}$ dumbbells interconnect $\infty^2\{[M_4O_4]^{4+}\}$ layers. These layers are composed of three crystallographically different, distorted $[OM_4]^{10+}$ tetrahedra, which are linked via four common edges. The compounds exhibit strong Raman active modes at around 215 cm^{-1} , which can be assigned to the Se–Se stretching vibration. Optical band gaps for $La_4O_4Se[Se_2]$, $Ce_4O_4Se[Se_2]$, $Pr_4O_4Se[Se_2]$, $Nd_4O_4Se[Se_2]$, and $Sm_4O_4Se[Se_2]$ were derived from diffuse reflectance spectra. The energy values at which absorption takes place are typical for semiconducting materials. For the compounds $M_4O_4Se[Se_2]$ ($M = La, Pr, Nd, Sm$) the fundamental band gaps, caused by transitions from the valence band to the conduction band (VB–CB), lie around 1.9 eV, while for $M = Ce$ an absorption edge occurs at around 1.7 eV, which can be assigned to f-d transitions of Ce^{3+} . Magnetic susceptibility measurements of $Ce_4O_4Se[Se_2]$ and $Nd_4O_4Se[Se_2]$ show Curie–Weiss behavior above 150 K with derived experimental magnetic moments of 2.5 μ_B/Ce and 3.7 μ_B/Nd and Weiss constants of $\theta_p = -64.9$ K and $\theta_p = -27.8$ K for the cerium and neodymium compounds, respectively. Down to 1.8 K no long-range magnetic ordering could be detected. Thus, the large negative values for θ_p indicate the presence of strong magnetic frustration within the compounds, which is due to the geometric arrangement of the magnetic sublattice in form of $[OM_4]^{10+}$ tetrahedra.

Introduction

Oxide selenides of the trivalent rare-earth metals are closely related to the corresponding oxide sulfides, which are currently used in technical applications, for example as phosphors in X-ray imaging detectors.¹ Like the oxide sulfides, rare-earth metal(III) oxide selenides are known to occur in different forms with various oxygen to selenium

ratios. On the one hand there are those comprising less oxygen than selenium for example $Pr_{10}OSe_{14}$ and $Pr_2OSe_2^{2-}$ and on the other hand one finds oxygen-rich compounds with empirical formulas M_2O_2Se and $M_4O_4Se_3$, such as $Sm_2O_2Se^3$

* To whom correspondence should be addressed. E-mail: schleid@iac.uni-stuttgart.de. Fax: +49(0)711/685-64241.

[†] Universitaet Stuttgart.

[‡] Colorado State University.

(1) (a) Kandarakis, I.; Cavouras, D. *Appl. Radiat. Isot.* **2001**, *54*, 821–831. (b) Kandarakis, I.; Cavouras, D. *Nucl. Instrum. Methods Phys. Res., Sect. A* **2001**, *460*, 412–423. (c) Kandarakis, I.; Cavouras, D. *Eur. J. Radiol.* **2001**, *11*, 1083–1091.

(2) Weber, F. A.; Schleid, Th. *Z. Anorg. Allg. Chem.* **2001**, *627*, 1383–1388.

(3) Eick, H. A. *Acta Crystallogr.* **1960**, *13*, 161.

and $La_4O_4Se_3$.⁴ Among those different rare-earth metal(III) oxide selenides, the members of the $M_4O_4Se_3$ family take an exceptional position because they contain more complex diselenide units $[Se_2]^{2-}$, in addition to Se^{2-} anions, as a structural component. Moreover, edge sharing $[OM_4]^{10+}$ tetrahedra, which form layers, constitute another structural key-element of these oxide selenides. Because magnetic sites, arranged in such tetrahedral motifs, can lead to geometric magnetic frustration, which suppresses long-range magnetic ordering of spins,⁵ the structural organization of $[OM_4]^{10+}$ tetrahedra plays an important role for the magnetic behavior of those compounds. Furthermore, at present, neither the corresponding sulfur containing compounds nor the tellurium counterparts of the $M_4O_4Se_3$ representatives are known; thus, the oxide selenides of the formula $M_4O_4Se_3$ are unique within the entire oxide chalcogenide family. Reports about the single crystal structure of $La_4O_4Se_3$,⁴ $Ce_4O_4Se_3$,⁶ and $Pr_4O_4Se_3$ ² are known, but less is known about the rest of the lanthanoid series, their physical properties, especially the magnetic behavior, and how the characteristics of those samples change with variation of the M^{3+} cation.

In this paper, a series of compounds of the formula type $M_4O_4Se[Se_2]$ ($M = La, Ce, Pr, Nd, Sm$) are studied. Crystal structures for $La_4O_4Se[Se_2]$, $Ce_4O_4Se[Se_2]$, $Pr_4O_4Se[Se_2]$, $Nd_4O_4Se[Se_2]$, and $Sm_4O_4Se[Se_2]$ are determined, and the influence of the M^{3+} cation on local building blocks and global parameters, such as unit cell dimensions for example, is investigated. Furthermore, optical properties of the $M_4O_4Se[Se_2]$ representatives ($M = La, Ce, Pr, Nd, Sm$) along with magnetic properties of $Ce_4O_4Se[Se_2]$ and $Nd_4O_4Se[Se_2]$ are reported.

Experimental Section

Synthesis. The compounds $M_4O_4Se[Se_2]$ ($M = La, Ce, Pr, Nd, Sm$) form by solid state reactions of the corresponding rare-earth metal, elemental selenium, and selenium dioxide (SeO_2). To synthesize $M_4O_4Se[Se_2]$ ($M = La, Ce, Pr, Nd, Sm$), mixtures of 1 mmol rare-earth metal (Cerac, 99.9%), 1/4 mmol (19.8 mg) selenium (Sigma Aldrich, 99.99%), and 1/2 mmol (55.5 mg) selenium dioxide (SeO_2 ; Sigma Aldrich, 99.99%) were loaded into fused silica ampoules under an inert argon atmosphere. The evacuated and sealed ampoules were heated to 750 °C at a rate of 25 K/h and kept at that temperature for 168 h. Afterward the samples were cooled to room temperature at a rate of 5 K/h. The microcrystalline products were examined by powder X-ray diffraction (XRD) and no byproduct could be detected for $M = Ce, Pr, Nd, Sm$. For $M = La$, however, a minor impurity phase was apparent in the powder XRD pattern, along with the desired $La_4O_4Se[Se_2]$. To obtain crystals that are big enough for single-crystal structure analyses, cesium iodide (CsI: Alfa Aesar, 99.9%) was added to the starting materials as a fluxing agent. After washing those samples with deionized water to eliminate additional cesium iodide, platelet-shaped light brown ($La_4O_4Se[Se_2]$), dark red ($Ce_4O_4Se[Se_2]$), olive green ($Pr_4O_4Se[Se_2]$), dark purple ($Nd_4O_4Se[Se_2]$), and brown ($Sm_4O_4Se[Se_2]$) crystals were selected for

single-crystal XRD analysis. However, this synthesis method yielded crystals that grow as inversion twins. Analogous attempts to obtain the corresponding europium and gadolinium compounds did not yield the intended products $Eu_4O_4Se[Se_2]$ and $Gd_4O_4Se[Se_2]$. In both cases, the “regular” oxide selenides M_2O_2Se ($M = Eu, Gd$) are formed exclusively under the depicted reaction conditions.

Crystal Structure Analysis. XRD data were collected on a Nonius Kappa CCD instrument and integrated with the program Denzo/Scapecapack⁷ or a Stoe image plate IPDS diffractometer and integrated with the program STOE REDU 4, respectively. The crystal structures of the compounds $M_4O_4Se[Se_2]$ ($M = La, Ce, Pr, Nd, Sm$) were solved by direct methods using SHELXS-97.⁸ Full-matrix least-squares refinement against $|F|^2$ was carried out using SHELXL-97,⁹ and the program HABITUS¹⁰ was used for absorption correction. All crystals were refined as inversion twins. Crystallographic data for $M_4O_4Se[Se_2]$ ($M = La, Ce, Pr, Nd, Sm$) are given in Table 1, whereas the final atomic coordinates for those compounds are listed in Table 2. Further details of the crystal structure analyses may be obtained from the Fachinformationszentrum Karlsruhe, D-76344 Eggenstein-Leopoldshafen, Germany (e-mail: crysdata@fiz-karlsruhe.de) on quoting the depository numbers CSD-419128 for $La_4O_4Se[Se_2]$, CSD-419127 for $Ce_4O_4Se[Se_2]$, CSD-94416 for $Pr_4O_4Se[Se_2]$, CSD-419129 for $Nd_4O_4Se[Se_2]$, and CSD-419130 for $Sm_4O_4Se[Se_2]$.

Raman Spectroscopy. The bulk solid-state Raman spectra of $M_4O_4Se[Se_2]$ ($M = La, Ce, Nd, Sm$) were recorded on a Nicolet Magna-IR 760 spectrometer with FT-Raman module attachment by use of a Nd:YAG excitation laser (1064 nm).

UV–vis Spectroscopy. Diffuse reflectance spectra were measured on a Varian Cary 500 Scan UV–vis–NIR spectrophotometer equipped with a Praying Mantis accessory. As reference, a Teflon standard was used. To convert reflectance into absorbance and obtain band gap information, the Kubelka–Munk function was applied.^{11,12}

Magnetic Measurements. Magnetic susceptibilities of $Ce_4O_4Se[Se_2]$ and $Nd_4O_4Se[Se_2]$ were measured at 0.5 T over a temperature range of 1.8–300 K with a Quantum Design SQUID magnetometer. The samples (about 65 mg $Ce_4O_4Se[Se_2]$ and 40 mg $Nd_4O_4Se[Se_2]$) were loaded in gelatin capsules and mounted in plastic capillaries for magnetic measurements.

Results and Discussion

Crystal Structure Description. The isostructural rare-earth metal(III) oxide selenides $M_4O_4Se[Se_2]$ ($M = La, Ce, Pr, Nd, Sm$) crystallize in the *non*-centrosymmetric orthorhombic space group *Amm*2 ($a = 857.94(7)$, $b = 409.44(4)$, $c = 1316.49(8)$ pm for $La_4O_4Se[Se_2]$; $a = 851.37(6)$, $b = 404.82(3)$, $c = 1296.83(9)$ pm for $Ce_4O_4Se[Se_2]$; $a = 849.92(6)$, $b = 402.78(3)$, $c = 1292.57(9)$ pm for $M = Pr_4O_4Se[Se_2]$; $a = 845.68(4)$, $b = 398.83(2)$, $c = 1282.45(7)$ pm for $Nd_4O_4Se[Se_2]$; and $a = 840.08(5)$, $b = 394.04(3)$,

(4) Dugué, J.; Adolphe, C.; Khodadad, P. *Acta Crystallogr. B* **1970**, *26*, 1627–1628.

(5) Greedan, J. E. *J. Mater. Chem.* **2001**, *11*, 37–53.

(6) Folchnandt, M.; Schleid, Th. *Z. Kristallogr.* **1998**; Supplement Issue No. 15, 84.

(7) Otwinowski, Z.; Minor, W. *Methods Enzymol.* **1997**, *276*, 307–326.

(8) Sheldrick, G. M. *SHELXS-97 Programs for X-ray Crystal Structure Solution* University of Göttingen Göttingen, Germany, 1997.

(9) Sheldrick, G. M. *SHELXL-97 Programs for X-ray Crystal Structure Refinement*; University of Göttingen: Göttingen, Germany, 1997.

(10) Herrendorff, W. *HABITUS Programm zur Optimierung der Kristallgestalt für die numerische Absorptionskorrektur*; Universität of Giessen: Giessen, Germany, 1995.

(11) (a) Kotum, G. *Reflectance Spectroscopy*; Springer-Verlag: New York, 1969. (b) Yamashita, N. *J. Phys. Soc. Jpn.* **1973**, *35*, 1089.

(12) Wendlandt, W. W.; Hecht, H. G. *Reflectance Spectroscopy*; Interscience Publishers: New York, 1966.

Table 1. Crystallographic Data for $M_4O_4Se[Se_2]$ (M = La, Ce, Pr, Nd, Sm)

	$La_4O_4Se[Se_2]$	$Ce_4O_4Se[Se_2]$	$Pr_4O_4Se[Se_2]$	$Nd_4O_4Se[Se_2]$	$Sm_4O_4Se[Se_2]$
empirical formula	$La_4O_4Se[Se_2]$	$Ce_4O_4Se[Se_2]$	$Pr_4O_4Se[Se_2]$	$Nd_4O_4Se[Se_2]$	$Sm_4O_4Se[Se_2]$
formula weight (in g/mol)	856.52	861.36	864.52	877.84	902.28
crystal system	orthorhombic	orthorhombic	orthorhombic	orthorhombic	orthorhombic
space group	$Amm2$	$Amm2$	$Amm2$	$Amm2$	$Amm2$
Z	2	2	2	2	2
unit cell dimensions (in pm)					
<i>a</i>	857.94(7)	851.37(6)	849.92(6)	845.68(4)	840.08(5)
<i>b</i>	409.44(4)	404.82(3)	402.78(3)	398.83(2)	394.04(3)
<i>c</i>	1316.49(8)	1296.83(9)	1292.57(9)	1282.45(7)	1263.83(6)
molar volume (in cm ³ /mol)	139.25	134.58	133.24	130.24	125.97
calculated density (in g/cm ³)	6.151	6.400	6.489	6.740	7.163
crystal size (in mm ³)	$0.09 \times 0.05 \times 0.03$	$0.11 \times 0.06 \times 0.03$	$0.10 \times 0.06 \times 0.04$	$0.10 \times 0.07 \times 0.06$	$0.12 \times 0.07 \times 0.05$
temperature (in K)	298	296	293	293	293
radiation	Bruker-Nonius Kappa CCD	Stoe IPDS image-plate	Stoe IPDS image-plate	Bruker-Nonius Kappa CCD	Bruker-Nonius Kappa CCD
theta range for data collection	$\lambda = 71.07$ pm (Mo K α)	$\lambda = 71.07$ pm (Mo K α)	$\lambda = 71.07$ pm (Mo K α)	$\lambda = 71.07$ pm (Mo K α)	$\lambda = 71.07$ pm (Mo K α)
index ranges (<i>hkl</i>)	$2.4^\circ \leq \theta \leq 27.5^\circ$	$3.1^\circ \leq \theta \leq 32.9^\circ$	$3.1^\circ \leq \theta \leq 32.9^\circ$	$3.2^\circ \leq \theta \leq 27.5^\circ$	$2.4^\circ \leq \theta \leq 27.4^\circ$
	$-11 \leq h \leq 11,$	$-12 \leq h \leq 12,$	$-11 \leq h \leq 11,$	$-10 \leq h \leq 10,$	$-10 \leq h \leq 10,$
	$-5 \leq k \leq 5,$	$-5 \leq k \leq 5,$	$-6 \leq k \leq 6,$	$-5 \leq k \leq 5,$	$-5 \leq k \leq 5,$
	$-16 \leq l \leq 16$	$-19 \leq l \leq 19$	$-19 \leq l \leq 19$	$-16 \leq l \leq 16$	$-16 \leq l \leq 16$
absorption coefficient μ (in mm ⁻¹)	29.87	32.16	33.93	36.19	40.66
extinction coefficient <i>g</i>	0.0009(1)	0.0410(15)	0.0058(3)	0.0143(5)	0.0049(3)
overall batch scale factor (BASF)	0.22(5)	0.29(4)	0.22(4)	0.01(7)	0.37(9)
reflections collected	3757	3245	4089	3493	3229
independent reflections	642	913	906	600	585
number of reflections <i>n</i> with $ F_o \geq 4\sigma(F_o)$	600	899	879	581	582
R_{int}/R_σ	0.077/0.041	0.028/0.020	0.066/0.039	0.066/0.036	0.058/0.031
Goof	1.104	1.047	1.041	1.057	1.124
R_1/wR_2 (for all data)	0.032/0.058	0.028/0.072	0.030/0.065	0.024/0.049	0.025/0.059
R_1 (for <i>n</i> data)	0.028	0.028	0.029	0.023	0.025
electron density peak/hole (in $e \times 10^{-6} \times \text{pm}^{-3}$)	2.33/-1.42	2.30/-2.28	2.25/-2.61	0.99/-1.48	1.33/-1.68

Table 2. Atomic Coordinates and Equivalent Isotropic Thermal Displacement Parameters (U_{eq} in pm^2) for $M_4O_4Se[Se_2]$ ($M = \text{La, Ce, Pr, Nd, Sm}$)

	Wyckoff position	x/a	y/b	z/c	U_{eq}^a
$La_4O_4Se[Se_2]$					
La1	2a	0	0	0^b	120(3)
La2	2b	1/2	0	0.01807(8)	112(3)
La3	4c	0.23641(9)	0	0.68560(5)	114(2)
Se1	4c	0.3569(2)	0	0.3573(1)	167(3)
Se2	2a	0	0	0.3115(2)	156(5)
O1	4c	0.2438(10)	0	0.0897(10)	119(27)
O2	2a	0	0	0.5871(12)	181(36)
O3	2b	1/2	0	0.6169(11)	140(35)
$Ce_4O_4Se[Se_2]$					
Ce1	2a	0	0	0^b	43(2)
Ce2	2b	1/2	0	0.01879(6)	40(2)
Ce3	4c	0.23613(7)	0	0.68561(4)	42(2)
Se1	4c	0.3555(2)	0	0.35772(9)	88(2)
Se2	2a	0	0	0.3117(1)	75(3)
O1	4c	0.2446(7)	0	0.0877(8)	70(17)
O2	2a	0	0	0.5861(8)	56(19)
O3	2b	1/2	0	0.6179(9)	67(21)
$Pr_4O_4Se[Se_2]$					
Pr1	2a	0	0	0^b	58(2)
Pr2	2b	1/2	0	0.01874(8)	52(2)
Pr3	4c	0.23639(7)	0	0.68482(6)	57(1)
Se1	4c	0.3550(2)	0	0.3567(1)	99(2)
Se2	2a	0	0	0.3108(1)	88(3)
O1	4c	0.2434(8)	0	0.0895(6)	80(17)
O2	2a	0	0	0.5853(8)	77(19)
O3	2b	1/2	0	0.6178(8)	84(19)
$Nd_4O_4Se[Se_2]$					
Nd1	2a	0	0	0^b	121(3)
Nd2	2b	1/2	0	0.01861(7)	116(3)
Nd3	4c	0.23628(8)	0	0.68420(5)	120(2)
Se1	4c	0.3550(2)	0	0.3566(1)	159(3)
Se2	2a	0	0	0.3115(2)	154(4)
O1	4c	0.2412(9)	0	0.0876(10)	109(22)
O2	2a	0	0	0.5856(12)	183(33)
O3	2b	1/2	0	0.6175(12)	166(32)
$Sm_4O_4Se[Se_2]$					
Sm1	2a	0	0	0^b	119(3)
Sm2	2b	1/2	0	0.01838(7)	111(3)
Sm3	4c	0.23650(8)	0	0.68272(5)	111(2)
Se1	4c	0.3545(2)	0	0.3557(1)	157(3)
Se2	2a	0	0	0.3108(2)	158(4)
O1	4c	0.2456(10)	0	0.0875(10)	122(27)
O2	2a	0	0	0.5868(13)	159(40)
O3	2b	1/2	0	0.6150(11)	87(30)

^a U_{eq} is defined as one-third of the trace of the orthogonalized U_{ij} tensor.

^b Arbitrarily fixed for origin definition.

$c = 1263.83(6)$ pm for $Sm_4O_4Se[Se_2]$) with two formula units per unit cell. In their crystal structures, two-dimensionally linked $\{[M_4O_4]^{4+}\}$ layers, which are interconnected by Se^{2-} anions and $[Se-Se]^{2-}$ dumbbells, hold three crystallographically distinct O^{2-} anions as well as three crystallographically different M^{3+} cations (Figure 1).

Each of these O^{2-} anions is surrounded by four M^{3+} cations in the shape of a distorted $[OM_4]^{10+}$ tetrahedron. To determine the degree of distortion in these $[OM_4]^{10+}$ polyhedra, a value, $\Delta(\text{dis})$, can be calculated barely based on the theory of continuous symmetry measures.¹³ $\Delta(\text{dis})$ gives the average square deviation of the real polyhedron from an ideal tetrahedron and takes discrepancies in distances, as well as in angles, into consideration. A perfect tetrahedron

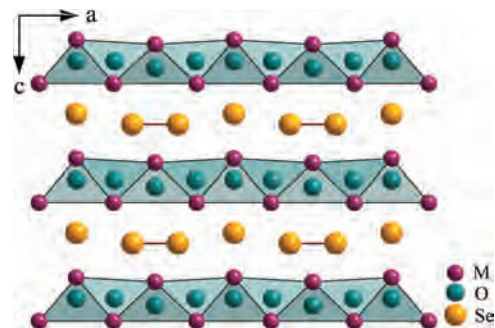


Figure 1. Perspective view of the crystal structure of $M_4O_4Se[Se_2]$ ($M = \text{La, Ce, Pr, Nd, Sm}$) along the b -axis.

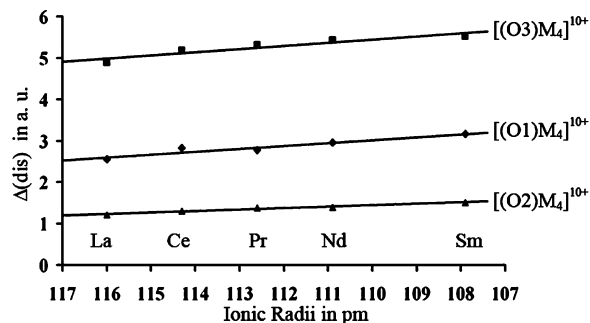


Figure 2. Degree of distortion, $\Delta(\text{dis})$, of the tetrahedral $[OM_4]^{10+}$ building blocks in the crystal structure of $M_4O_4Se[Se_2]$ ($M = \text{La, Ce, Pr, Nd, Sm}$). Calculation is based on a model that gives the square deviation from an ideal tetrahedron.

(normalized to the size of the distorted polyhedron) is superimposed over the actual figure found in the crystal structure. Then, the average root-mean-square deviation between the two polyhedra is calculated and multiplied by 100 to obtain a convenient value for $\Delta(\text{dis})$. A more detailed description of the calculation of $\Delta(\text{dis})$ is given in the Supporting Information. From this it follows that a polyhedron is all the more distorted the higher the value for $\Delta(\text{dis})$ gets. By using this method, it is found that among the three different $[OM_4]^{10+}$ entities, $[(O2)M_4]^{10+}$ deviates the least from a perfect tetrahedron, followed by $[(O1)M_4]^{10+}$ and $[(O3)M_4]^{10+}$, which is the most distorted one. Furthermore, the degree of distortion $\Delta(\text{dis})$ increases slightly with decreasing size of the rare-earth metal cation (Figure 2). Although the distances $d(M-O)$ within the tetrahedra vary the most within the least contorted $[(O2)M_4]^{10+}$ units (see Table 3), the angles in the $[OM_4]^{10+}$ units, which deviate significantly from the ideal tetrahedral angle of 109.47° (e.g., $Sm_4O_4Se[Se_2]$ $\angle(M-O-M) = 101-138^\circ$, see Table 3 for details), turn out to play a more decisive role for the degree of distortion in the three crystallographically different tetrahedra.

The above-described $[OM_4]^{10+}$ building units are well-known structural features in many different rare-earth metal(III) oxide chalcogenides, for example $M_{10}OS_{14}$ ($M = \text{La, Ce, Pr, Nd, Sm}$),¹⁴ Dy_2OS_2 -I and -II,¹⁵ Nd_2O_2S ,¹⁶ Pr_2O_2Se ,²

(13) (a) Zabrodsky, H.; Peleg, S.; Avnir, D. *J. Am. Chem. Soc.* **1992**, *114*, 7843–7851. (b) Ok, K. M.; Halasyamani, P. S.; Casanova, D.; Llundell, M.; Alemany, P.; Santiago, A. *Chem. Mater.* **2006**, *18*, 3176–3183.

(14) Lissner, F.; Schleid, Th. *J. Less-Common Met.* **1991**, *175*, 309–319. (15) Schleid, Th. *Z. Anorg. Allg. Chem.* **1991**, *602*, 39–47. (16) Lissner, F.; Schleid, Th. *Z. Kristallogr.* **1993**, *205*, 117–118.

Table 3. Selected Bond Distances (d in pm) and Angles (\angle in deg) for $M_4O_4Se[Se_2]$ ($M = La, Ce, Pr, Nd, Sm$)

	$La_4O_4Se[Se_2]$	$Ce_4O_4Se[Se_2]$	$Pr_4O_4Se[Se_2]$	$Nd_4O_4Se[Se_2]$	$Sm_4O_4Se[Se_2]$
Distances					
M1–O2 ($2\times$) ^{a,b}	234.7(8)	231.2(5)	229.6(5)	227.6(7)	225.5(8)
M1–O1 ($2\times$) ^c	240.2(9)	237.3(7)	237.0(7)	232.9(9)	234.1(9)
M1–Se2 ($2\times$) ^{a,b}	321.7(2)	317.2(1)	316.8(1)	313.4(2)	309.8(2)
M2–O1 ($2\times$) ^d	239.2(9)	235.1(7)	236.5(8)	236.1(9)	230.9(9)
M2–O3 ($2\times$) ^{a,b}	242.6(7)	239.7(6)	238.6(7)	236.3(8)	231.8(8)
M2–Se1 ($4\times$) ^{b,e,f,a}	319.0(2)	315.8(1)	315.6(1)	313.0(2)	309.9(2)
M3–O1 ($2\times$) ^{g,h}	240.6(7)	238.9(6)	236.2(6)	234.8(7)	231.0(7)
M3–O2	240.7(8)	239.1(6)	238.6(6)	236.5(8)	232.7(8)
M3–O3	243.6(5)	241.2(4)	240.2(4)	238.9(5)	237.3(5)
M3–Se1 ($2\times$) ^{h,g}	322.0(2)	318.0(1)	316.4(1)	314.2(2)	310.5(2)
M3–Se2 ($2\times$) ^{g,h}	332.5(2)	328.8(1)	327.8(1)	326.1(2)	323.2(1)
Se1–Se1	245.6(3)	246.1(4)	246.5(4)	245.3(4)	244.6(4)
Angles					
M1–O1–M2	127.4(5)	129.0(5)	128.1(4)	129.1(2)	129.6(5)
M1–O1–M3 ($2\times$) ^{a,b}	103.6(2)	103.2(2)	103.4(2)	103.8(6)	102.5(2)
M2–O1–M3 ($2\times$) ^{a,b}	103.4(2)	103.3(2)	103.0(2)	102.4(2)	103.2(2)
M3 ^a –O1–M3 ^b	116.6(5)	115.7(4)	116.9(3)	116.3(2)	117.2(4)
M1 ^g –O2–M1 ^h	121.5(3)	122.2(5)	122.5(3)	122.3(7)	121.8(5)
M1 ^{g,h} –O2–M3 ($4\times$) ^c	105.3(3)	105.1(1)	105.0(2)	104.9(3)	104.7(3)
M3 ^c –O2–M3	114.8(6)	114.6(4)	114.8(2)	115.3(6)	117.2(7)
M2 ^g –O3–M2 ^h	115.1(6)	115.2(5)	115.3(2)	115.1(6)	116.4(5)
M2 ^{g,h} –O3–M3 ($4\times$) ^d	101.5(1)	101.3(1)	101.2(2)	101.1(1)	101.0(1)
M3–O3–M3 ^h	136.4(7)	137.3(5)	137.5(3)	138.0(5)	137.7(6)

Symmetry transformations used to generate equivalent atoms: ^a: $x, y + 1/2, z - 1/2$. ^b: $x, y - 1/2, z - 1/2$. ^c: $-x, -y, z$. ^d: $-x + 1, -y, z$. ^e: $-x + 1, -y - 1/2, z - 1/2$. ^f: $-x + 1, -y + 1/2, z - 1/2$. ^g: $x, y - 1/2, z + 1/2$. ^h: $x, y + 1/2, z + 1/2$.

and M_2O_2Te ($M = La-Nd, Sm-Ho$).¹⁷ It is also found that the degree of tetrahedral cross-linking in those compounds increases with increasing oxygen content,² whereas in oxide chalcogenides with similar oxygen content (M_2O_2Ch ; $Ch = S, Se, Te$) the degree of interconnection decreases with diminishing size of the chalcogenide anion. Thus, in the isostructural trigonal compounds M_2O_2S and M_2O_2Se ($M = rare-earth\ metal$) the $[OM_4]^{10+}$ tetrahedra are interconnected via three common edges to form two-dimensional double layers, which leave space for holes, whereas in M_2O_2Te ($M = La-Nd, Sm-Ho$) $[OM_4]^{10+}$ tetrahedra share four common edges, and therefore, more compact two-dimensionally linked layers are formed.

As the oxygen content of the compounds described in this paper is comparable to M_2O_2Ch ($2 \times M_2O_2Ch = M_4O_4Ch_2$; $Ch = S, Se, Te$) and since Se^{2-} anions as well as the bigger $[Se_2]^{2-}$ dumbbells are present, it is not surprising that in the crystal structures of $M_4O_4Se[Se_2]$ ($M = La, Ce, Pr, Nd, Sm$) $[OM_4]^{10+}$ tetrahedra connect in the same way as in M_2O_2Te , that is, via four common edges (Figure 3).

Nevertheless, the overall alignment of the ${}^2_{\infty}\{[M_4O_4]^{4+}\}$ layers in $M_4O_4Se[Se_2]$ ($M = La, Ce, Pr, Nd, Sm$) and M_2O_2Te is different, and thus, the two compounds are neither isostructural nor exhibit a real group–subgroup relationship of the two crystal structures, although, the unit cell dimensions of $M_4O_4Se[Se_2]$ ($Amm2$, e.g., $La_4O_4Se[Se_2]$: $a = 857.94(7)$, $b = 409.44(4)$, $c = 1316.49(8)$ pm) are approximately twice the size of M_2O_2Te ($I4/mmm$, e.g., La_2O_2Te : $a = b = 412.31(4)$, $c = 1309.6(1)$ pm¹⁷). In M_2O_2Te ($M = La-Nd, Sm-Ho$)¹⁷ the ${}^2_{\infty}\{[M_4O_4]^{4+}\}$ arrangements pile along the c -axis in such a way that they are reflected by a mirror plane perpendicular to $[001]$; therefore,

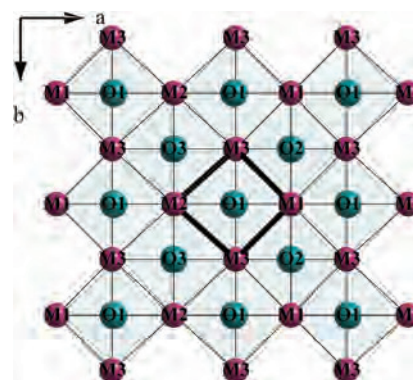


Figure 3. View of the ${}^2_{\infty}\{[M_4O_4]^{4+}\}$ layers formed by edge-sharing $[OM_4]^{10+}$ tetrahedra in the crystal structure of $M_4O_4Se[Se_2]$ ($M = La, Ce, Pr, Nd, Sm$) along the c -axis. Common edges are emphasized in dark color.

M^{3+} cations are situated above M^{3+} cations and O^{2-} anions above O^{2-} anions, whereas in $M_4O_4Se[Se_2]$ ($M = La, Ce, Pr, Nd, Sm$) every second ${}^2_{\infty}\{[M_4O_4]^{4+}\}$ layer is shifted by $1/2$ the length of the b -axis; thus, M^{3+} cations are located above O^{2-} anions and vice versa (Figure 4).

As a result, the coordination number of the linking Se^{2-} and $[Se-Se]^{2-}$ anions in $M_4O_4Se[Se_2]$ ($M = La, Ce, Pr, Nd, Sm$) is six, like the coordination number of Se^{2-} anions in M_2O_2Se , but not eight, which is the coordination number of Te^{2-} anions in M_2O_2Te . Nevertheless, in contrast to M_2O_2Se where the Se^{2-} anions feature a trigonal antiprismatic coordination sphere, in $M_4O_4Se[Se_2]$ the six M^{3+} cations around the $(Se_2)^{2-}$ and $[(Se1)-(Se1)]^{2-}$ units form a triangular prism. However, in the $[(Se1)_2M_6]^{16+}$ building blocks, the barycenter of the dumbbell-like $[Se-Se]^{2-}$ anion is situated in the middle of the triangular prism, and the nuclei of the actual atoms reside in a rectangular face of the prism (Figure 5).

(17) Weber, F. A.; Schleid, Th. *Z. Anorg. Allg. Chem.* **1999**, *625*, 1833–1838.

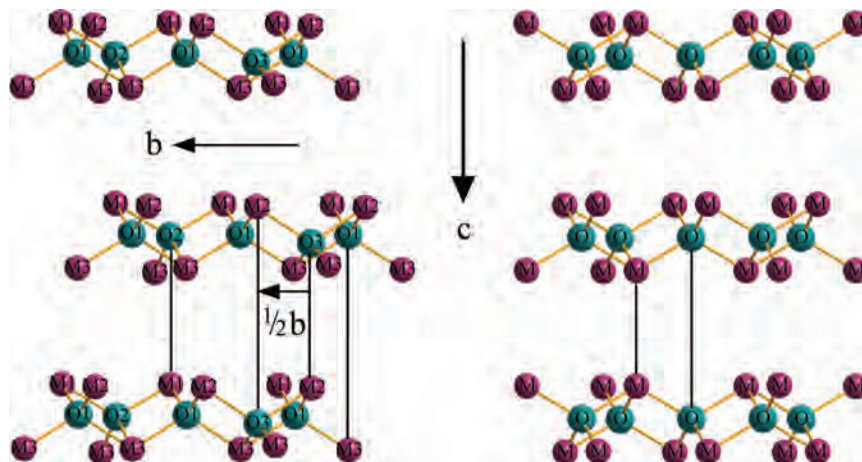


Figure 4. Comparison of the two types of compounds $M_4O_4Se[Se_2]$ (left) and M_2O_2Te (right) ($M = La, Ce, Pr, Nd, Sm$), showing the two different ways of ${}^2_{\infty}\{[M_4O_4]^{4+}\}$ layer stacking. Black lines indicate superimposed atoms.

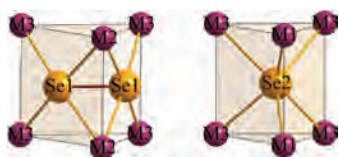


Figure 5. Representation of the coordination spheres of $[Se-Se]^{2-}$ units and Se^{2-} anions in $M_4O_4Se[Se_2]$ ($M = La, Ce, Pr, Nd, Sm$).



Figure 6. Representation of the coordination spheres of the three crystallographically different M^{3+} cations in $M_4O_4Se[Se_2]$ ($M = La, Ce, Pr, Nd, Sm$).

For a given metal cation (e.g. Sm), the six distances between the M^{3+} cations and Se atoms of the diselenide units have almost the same length ($d(Se1-Sm2) = 310$ pm ($2\times$), $d(Se1-Sm3) = 311$ pm ($4\times$)), whereas in the Se^{2-} centered $[(Se_2)M_6]^{16+}$ prisms two shorter and four longer bonds appear ($d(Se2-Sm1) = 310$ pm ($2\times$), $d(Se2-Sm3) = 323$ pm ($4\times$)). In the whole series $M_4O_4Se[Se_2]$ ($M = La, Ce, Pr, Nd, Sm$), however, the bond lengths between Se anions and M^{3+} cations in both of these prisms decrease with shrinking radius of the M^{3+} cations from La, Ce, Pr, Nd, to Sm (Table 3). Contrary to the metal selenium bonds, the distance between the two Se atoms within the $[Se-Se]^{2-}$ dumbbells is hardly affected by the cationic radius of the trivalent rare-earth metal and the values for $d(Se-Se)$ range from 245 to 246 pm; $d_{La}(Se-Se) = 245.6$ pm, $d_{Ce}(Se-Se) = 246.1$ pm, $d_{Pr}(Se-Se) = 246.5$ pm, $d_{Nd}(Se-Se) = 245.3$ pm, $d_{Sm}(Se-Se) = 244.6$ pm.

The three crystallographically different M^{3+} cations, that set up the coordination spheres of $[(Se1)-(Se1)]^{2-}$ and $(Se2)^{2-}$, cover coordination numbers of $CN = 8$ for M2 and M3, but only $CN = 6$ for M1. In all three coordination polyhedra, four O^{2-} anions form a contorted square-like arrangement situated above the M^{3+} cation for M1 and M2 and beneath for M3, respectively (relative to the $[00\bar{1}]$ direction). For the 8-fold surrounded cations $(M2)^{3+}$ and $(M3)^{3+}$, the overall coordination polyhedron is completed by four selenium atoms, forming a rectangular antiprism. In the case of M2, two entire side-on attached $[Se-Se]^{2-}$ units are appended; whereas for M3, two Se^{2-} anions and two corner linked end-on grafted $[Se-Se]^{2-}$ dumbbells round off the coordination sphere. For the 6-fold coordinated $(M1)^{3+}$ cations, two additional Se^{2-} anions are situated directly above

two of the O^{2-} anions that form a quadrangle; thus, the coordination geometry around the $(M1)^{3+}$ cations resembles a square prism which is lacking two vertices (Figure 6).

As expected, the distances in the metal-chalcogen polyhedra shrink with the decreasing size of the M^{3+} cation, that is, $d(La-Ch) > d(Ce-Ch) > d(Pr-Ch) > d(Nd-Ch) > d(Sm-Ch)$ ($Ch = O, Se$), for example $d(La1-O1) = 240.2$, $d(La1-O2) = 234.7$, $d(La1-Se2) = 321.7$ pm as opposed to $d(Sm1-O1) = 234.1$, $d(Sm1-O2) = 225.5$, $d(Sm1-Se2) = 309.8$ pm. Thus, the unit cell dimensions for the compounds $M_4O_4Se[Se_2]$ ($M = La, Ce, Pr, Nd, Sm$) decrease as well. However, as both the b - and c -axes are reduced by about 4% from $La_4O_4Se[Se_2]$ to $Sm_4O_4Se[Se_2]$, the a -axis declines only about 2%. This reflects the alignment of the $[Se-Se]^{2-}$ dumbbells within the crystal structures of $M_4O_4Se[Se_2]$ ($M = La, Ce, Pr, Nd, Sm$). The $[Se-Se]^{2-}$ units, with almost consistent Se-Se distances throughout the five compounds, lie parallel to the a -axis; therefore, this axis is less affected by the changing size of the M^{3+} cations.

Physical Properties

Raman Spectroscopy. The four compounds $M_4O_4Se[Se_2]$ ($M = La, Ce, Nd, Sm$) exhibit comparable Raman spectra, as shown in Figure 7. They comprise a strong peak centered around 215 cm^{-1} along with some weak Raman bands at low and high energy sites of this strong peak. In the spectrum of $Ce_4O_4Se[Se_2]$, for example, three less-intense low energy peaks at 90, 125, and 162 cm^{-1} , the strong Raman band at 214 cm^{-1} , and a peak with feeble intensity at 278 cm^{-1} are detectable. Some of those peaks shift as the size of the rare-earth metal cation changes, whereas others are hardly affected. In the case of $La_4O_4Se[Se_2]$, two more small peaks

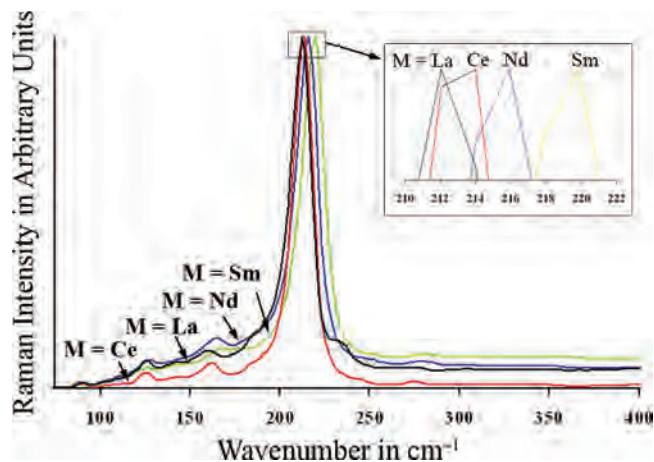


Figure 7. Raman spectra of $\text{La}_4\text{O}_4\text{Se}[\text{Se}_2]$ (black), $\text{Ce}_4\text{O}_4\text{Se}[\text{Se}_2]$ (red), $\text{Nd}_4\text{O}_4\text{Se}[\text{Se}_2]$ (blue), and $\text{Sm}_4\text{O}_4\text{Se}[\text{Se}_2]$ (green). The inset shows the shift of the strongest peak with decreasing radius of the lanthanoid trication.

are present at 185 and 233 cm^{-1} , which are due to an impurity phase in the sample. The simplicity of the Raman spectra implies that it can be explained based on a model of separated structural units or elements. Thus, the most prominent Raman bands at $\nu = 212 \text{ cm}^{-1}$ (for $M = \text{La}$), $\nu = 214 \text{ cm}^{-1}$ (for $M = \text{Ce}$), $\nu = 216 \text{ cm}^{-1}$ (for $M = \text{Nd}$), and $\nu = 220 \text{ cm}^{-1}$ (for $M = \text{Sm}$) can be assigned to the stretching vibration of the Se–Se bond in the $[\text{Se}–\text{Se}]^{2-}$ dumbbells. Compared to other compounds with $[\text{Se}–\text{Se}]^{2-}$ units like K_2Se_2 , Rb_2Se_2 ,¹⁸ and $\text{K}_2\text{Gd}_2\text{Sb}_2\text{Se}_9$ ¹⁹ which give resonance between 253 and 266 cm^{-1} for the Se–Se stretching vibration, the Raman active modes for $\text{M}_4\text{O}_4\text{Se}[\text{Se}_2]$ ($M = \text{La, Ce, Nd, Sm}$) are shifted toward lower energies, that is, the strength of the interactions between the two Se atoms in the $[\text{Se}–\text{Se}]^{2-}$ units declines in those compounds. This is a result of the differences in the cationic environment of the $[\text{Se}–\text{Se}]^{2-}$ dumbbells, since the Se–Se bond is influenced by the metal atom being bound to Se. In K_2Se_2 , Rb_2Se_2 , and $\text{K}_2\text{Gd}_2\text{Sb}_2\text{Se}_9$ the $[\text{Se}_2]^{2-}$ anions are surrounded by alkali metal cations or K^+ plus Gd^{3+} cations, respectively, whereas in $\text{M}_4\text{O}_4\text{Se}[\text{Se}_2]$ ($M = \text{La, Ce, Nd, Sm}$) the coordination sphere around the $[\text{Se}_2]^{2-}$ units consists exclusively of M^{3+} cations. Thus, in $\text{M}_4\text{O}_4\text{Se}[\text{Se}_2]$ ($M = \text{La, Ce, Nd, Sm}$) cations with a higher charge to radius ratio and therefore a higher *Coulomb* potential attract the Se atoms and expand the Se–Se bond, which also reveals in the length of the Se–Se bond, calculated from single-crystal XRD data, with values of $d(\text{Se}–\text{Se}) = 240 \text{ pm}$ for K_2Se_2 ¹⁸ and $\text{K}_2\text{Gd}_2\text{Sb}_2\text{Se}_9$ ¹⁹ compared to approximately 246 pm for $\text{M}_4\text{O}_4\text{Se}[\text{Se}_2]$ ($M = \text{La, Ce, Nd, Sm}$). Data for Rb_2Se_2 and Kb_2Se_2 , where one Raman band shifts from $\nu = 266 \text{ cm}^{-1}$ for Rb_2Se_2 to $\nu = 253 \text{ cm}^{-1}$ for K_2Se_2 ¹⁸ support this argument. Furthermore, in K_2S_2 with two distinct $[\text{S}–\text{S}]^{2-}$ units and distances of 211 and 214 pm, respectively, for $d(\text{S}–\text{S})$, a difference of about 3 pm in bond length gives two individual Raman modes for the S–S stretching vibra-

tions separated by about 22 cm^{-1} . Considering all of this, the observed shift of the Raman signal for the stretching vibration of the Se–Se bond in $\text{M}_4\text{O}_4\text{Se}[\text{Se}_2]$ ($M = \text{La, Ce, Nd, Sm}$) toward lower energies seems to be quite reasonable.

In the four Raman spectra of $\text{La}_4\text{O}_4\text{Se}[\text{Se}_2]$, $\text{Ce}_4\text{O}_4\text{Se}[\text{Se}_2]$, $\text{Nd}_4\text{O}_4\text{Se}[\text{Se}_2]$, and $\text{Sm}_4\text{O}_4\text{Se}[\text{Se}_2]$, the Se–Se stretching mode shifts toward higher wave numbers with decreasing radius of the M^{3+} cation. This seems to correlate with the Se–Se bond lengths derived from crystal structure calculations, which presumably decrease with the exception of $M = \text{Ce}$, from $M = \text{La}$ to Sm . Keeping in mind that the bond lengths for $M = \text{Ce}$ (and $M = \text{Pr}$, for which no Raman spectrum was measured) are difficult to compare with those of the other compounds, since the structural data of $\text{Ce}_4\text{O}_4\text{Se}[\text{Se}_2]$ (and $\text{Pr}_4\text{O}_4\text{Se}[\text{Se}_2]$) were collected on different diffractometers. On the other hand, the low energy peaks at 90 and 125 cm^{-1} are hardly affected by the change of the M^{3+} cation, whereas the two Raman modes around 165 and 275 cm^{-1} are influenced in the same way as seen for the strongest Raman band. According to previously reported Raman spectroscopic studies of oxide selenides and sulfides,²⁰ the less-intense Raman modes observed at 90, 125, 165, and 275 cm^{-1} in the spectra of $\text{M}_4\text{O}_4\text{Se}[\text{Se}_2]$ ($M = \text{La, Ce, Nd, Sm}$) can most likely be attributed to internal modes of the rare-earth metal(III) oxide selenide polyhedra, since external modes are expected to occur at even lower energies.

UV–vis Spectroscopy. Optical properties of the five compounds $\text{M}_4\text{O}_4\text{Se}[\text{Se}_2]$ ($M = \text{La, Ce, Pr, Nd, Sm}$) were examined by collecting UV–vis diffuse reflectance spectra. To get information about optical band gaps for the samples, diffuse reflectance was converted into absorption using the Kubelka–Munk approximation,¹² which relates the absorbance coefficient (α) and the diffusion coefficient (S) of the compounds. In Figure 8 plots of the Kubelka–Munk function (α/S) against energy are shown for $\text{La}_4\text{O}_4\text{Se}[\text{Se}_2]$, $\text{Ce}_4\text{O}_4\text{Se}[\text{Se}_2]$, $\text{Pr}_4\text{O}_4\text{Se}[\text{Se}_2]$, $\text{Nd}_4\text{O}_4\text{Se}[\text{Se}_2]$, and $\text{Sm}_4\text{O}_4\text{Se}[\text{Se}_2]$. Two steep absorption thresholds appear in the energy range of 0.5–5 eV (250–2500 nm). The threshold at lower energy can be assigned to the fundamental optical band gap of the sample. For the four different samples $\text{M}_4\text{O}_4\text{Se}[\text{Se}_2]$, the absorption edge energies (E_g), derived from the intersection point of the baseline along the energy axis and the extrapolated line of the linear part of the threshold, exhibit values of $E_g = 1.89 \text{ eV}$ for $M = \text{La}$, $E_g = 1.69 \text{ eV}$ for $M = \text{Ce}$, $E_g = 1.87 \text{ eV}$ for $M = \text{Pr}$, $E_g = 1.87 \text{ eV}$ for $M = \text{Nd}$, and $E_g = 1.88 \text{ eV}$ for $M = \text{Sm}$, typical for semiconducting materials. The band gaps widths of approximately 1.9 eV for $M = \text{La, Pr, Nd, Sm}$ and 1.7 eV for $M = \text{Ce}$ are comparable to the band gaps widths found for lanthanoid(III) sesquiselenides M_2Se_3 ($M = \text{La, Ce, Pr, Nd}$,

(18) Böttcher, P.; Gretzschmann, J.; Keller, R. *Z. Anorg. Allg. Chem.* **1993**, *619*, 476–488.

(19) Choi, K.-S.; Hanko, J. A.; Kanatzidis, M. G. *J. Solid State Chem.* **1999**, *147*, 309–319.

(20) (a) Barnier, S.; Julien, C.; Winterberger, M. *Mater. Res. Bull.* **1995**, *30*, 225–232. (b) Barnier, S.; Palazzi, M.; Guittard, M.; Julien, C. *J. Mater. Sci.* **1993**, *28*, 3761–3763. (c) Barnier, S.; Julien, C.; Guittard, M. *Spectrochim. Acta* **1988**, *44A*, 709–712. (d) Sourisseau, C.; Fouassier, M.; Mauricot, R.; Boucher, F.; Evain, M. *J. Raman Spectrosc.* **1997**, *28*, 973–978. (e) Sourisseau, C.; Cavagnat, R.; Mauricot, R.; Boucher, F.; Evain, M. *J. Raman Spectrosc.* **1997**, *28*, 965–971.

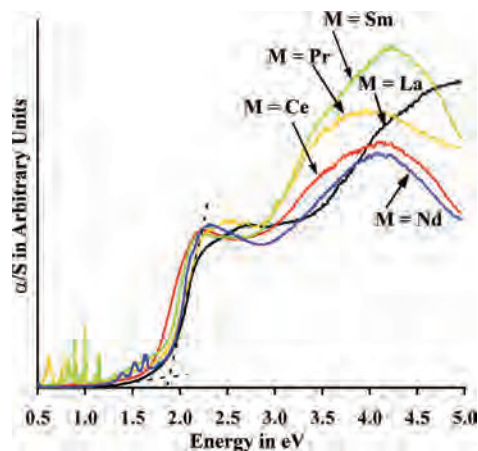


Figure 8. Diffuse reflectance spectra of $La_4O_4Se[Se_2]$ (black), $Ce_4O_4Se[Se_2]$ (red), $Pr_4O_4Se[Se_2]$ (yellow), $Nd_4O_4Se[Se_2]$ (blue) and $Sm_4O_4Se[Se_2]$ (green) after applying a Kubelka–Munk transformation. Dashed black lines show the derivation of E_g for $La_4O_4Se[Se_2]$ as an example.

Tb).²¹ In the case of $M = La, Pr, Nd,$ and Sm , the absorption edges are caused by a transition from the top of the valence band (VB) to the bottom of the conduction band (CB), where the uppermost part of the valence band can be presumably attributed to $Se(4p)$ states and the bottom of the conduction band results most likely from empty $M(5d)$ orbitals of the rare-earth metal cations ($M = La, Pr, Nd, Sm$). In $Ce_4O_4Se[Se_2]$, however, the occupied $4f$ bands are situated above the valence band, and the observed absorption edge is due to $Ce^{III}-4f^{15}d^0$ to $Ce^{III}-4f^{14}5d^1$ transitions. Thus, the band gap for $Ce_4O_4Se[Se_2]$ is significantly smaller, and the absorption edge is shifted to lower energy.

The second steep absorption thresholds in the plots of the Kubelka–Munk function (α/S) against energy for $M_4O_4Se[Se_2]$ (Figure 8) occur at 3.32 eV for $M = La$, 2.97 eV for $M = Ce$, 2.95 eV for $M = Pr$, 2.95 eV for $M = Nd$, and 2.89 eV for $M = Sm$. Unfortunately, the lanthanum sample is contaminated with an impurity phase; thus, the value for the second threshold is altered for $M = La$. This absorption at higher energies is most likely due to a transition from a group of valence bands with predominant $O(2p)$ character that lie below the top part of the valence band to the conduction band. Because band structure calculations for other rare-earth metal(III) oxide chalcogenides (e.g., La_2O_2S ,²² Sm_2O_2S , Eu_2O_2S ²³ and Y_2O_2S ²⁴) show that in oxide sulfides the valence band results from a mixing of S and O orbitals, it seems possible that in oxide selenides, where the mixing of Se and O orbitals becomes more difficult because of different energetic levels of these orbitals, Se and O orbitals cause separate energy levels within the valence band. Such an explanation should be handled with caution in the absence of a correct band structure calculation given that a comparison with band structure calculations for oxide sulfides can only lead to some speculations, since trigonal

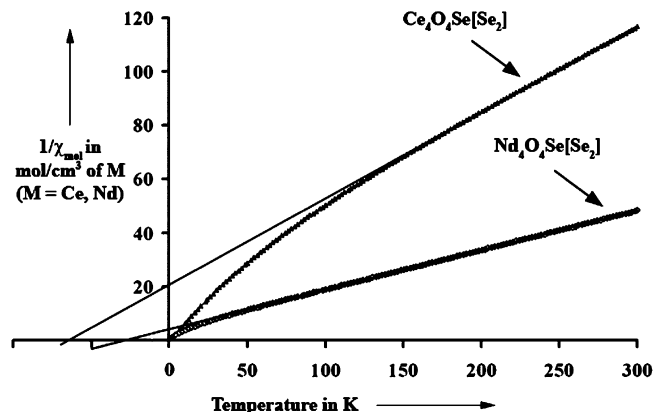


Figure 9. Temperature dependence of the inverse molar magnetic susceptibility for $Ce_4O_4Se[Se_2]$ and $Nd_4O_4Se[Se_2]$ at 0.5 T.

M_2O_2S and orthorhombic $M_4O_4Se[Se_2]$ have different crystal structures and thus different anionic sublattices.

Besides the two steep absorption thresholds attributed to valence to conduction band transitions, the diffuse reflectance spectra of $Pr_4O_4Se[Se_2]$, $Nd_4O_4Se[Se_2]$, and $Sm_4O_4Se[Se_2]$ show a series of characteristic lines between 0.5–1.0 eV for $M = Pr$, 1.3–1.7 eV for $M = Nd$, and 0.5–1.5 eV for $M = Sm$, which correspond to typical $f-f$ transitions for M^{3+} cations ($M = Pr, Nd, Sm$).²⁵ This indicates that the $4f$ electrons are strongly localized, and the optical band gaps of these compounds are only slightly influenced by the different cations in $M_4O_4Se[Se_2]$ ($M = La, Pr, Nd, Sm$). This is also evident in the derived absorption energies for the two optical transitions, which are almost the same for all four compounds $M_4O_4Se[Se_2]$ ($M = La, Ce, Nd, Sm$). Although, the energy values of the first threshold in $Ce_4O_4Se[Se_2]$ and the second absorption in $La_4O_4Se[Se_2]$ deviate, but that is due to $4f-5d$ transitions (for $M = Ce$) and a contamination of the sample (for $M = La$).

Magnetic Properties. Temperature dependence of reciprocal molar magnetic susceptibility ($1/\chi_{mol}$) for $Ce_4O_4Se[Se_2]$ and $Nd_4O_4Se[Se_2]$ at 0.5 T is shown in Figure 9. Both compounds deviate from an ideal Curie–Weiss behavior at lower temperatures, probably because of crystal field effects.²⁶ Nevertheless, fitting of the data to the Curie–Weiss law $\chi = C/(T - \theta_p)$ above 150 K yields an effective magnetic moment of $\mu_{eff} = 2.5 \mu_B/Ce$ and a Weiss constant of $\theta_p = -64.9$ K for $Ce_4O_4Se[Se_2]$ and $\mu_{eff} = 3.7 \mu_B/Nd$ and $\theta_p = -27.8$ K for $Nd_4O_4Se[Se_2]$, respectively. The derived effective moments are in good agreement with the theoretical values for the free cations in the trivalent oxidation state $\mu_{eff}(Ce^{3+}) = 2.54 \mu_B$ and $\mu_{eff}(Nd^{3+}) = 3.62 \mu_B$,²⁷ but the negative values for θ_p indicate predominant antiferromagnetic interactions in these compounds. However, there is no evidence of magnetic ordering down to 1.8 K. This is also

(21) Prokofiev, A. V.; Shelykh, A. I.; Golubkov, A. V.; Smirnov, I. A. *J. Alloys Compd.* **1995**, *219*, 172–175.

(22) Vali, R. *Comput. Mater. Sci.* **2006**, *37*, 300–305.

(23) Llanos, J.; Sánchez, V.; Mujica, C.; Buljan, A. *Mater. Res. Bull.* **2002**, *37*, 2285–2291.

(24) Mikami, M.; Oshiyama, A. *Phys. Rev. B* **1998**, *57*, 8939–8944.

(25) (a) Tejedor, P.; Hollander, F. J.; Fayos, J.; Stacy, A. M. *J. Cryst. Growth* **1995**, *155*, 223–228. (b) Van Deun, R.; Binnemans, K.; Görrler-Walrand, C.; Adam, J. L. *J. Alloys Compd.* **1999**, *283*, 59–65. (c) Oczko, G.; Macalink, L.; Legendziewicz, J.; Hanuza, J. *J. Alloys Compd.* **2004**, *380*, 327–336.

(26) Cascales, C.; Sáez-Puche, R.; Porcher, P. *J. Solid State Chem.* **1995**, *114*, 53–56.

(27) Smart, L.; Moore, E. *Solid State Chemistry*; Chapman & Hall: London, 1992.

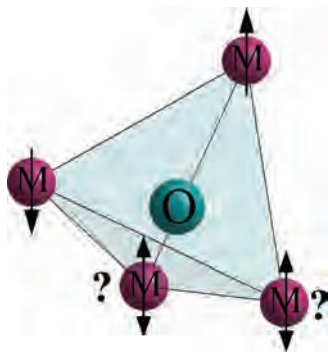


Figure 10. Representation of a $[OM_4]^{10+}$ tetrahedron showing geometric spin frustration. Only two of the four spin constraints can be satisfied at the same time.⁵

confirmed by the low field (0.001 T) data, for which the graph for the temperature dependent molar susceptibility (χ_{mol}) is absolutely asymptotic under both, field cooled (FC) and zero-field cooled (ZFC) conditions from 1.8–300 K. Thus, the large negative values for θ_p and the absence of any ordering are a sign of magnetic frustration in the systems. In addition, the absence of a FC and ZFC divergence at low field rules out the possibility of any spin glass state or frozen short-range ordering above 1.8 K in those compounds. Applying the so-called “frustration index” f ,^{5,28} that is, $f = |\theta_p|/T_x$ (where T_x is a spin ordering or spin freezing temperature, respectively) results in $f > 32$ for $Ce_4O_4Se[Se_2]$ and $f > 14$ for $Nd_4O_4Se[Se_2]$, which are indications for the presence of frustration, since a non-frustrated system is supposed to show values in the range of 2 to 5.⁵

Magnetic frustration often occurs in materials in which the magnetic sublattice is arranged in triangles (Kagome lattices) or tetrahedra (pyrochlore and spinel structures), since in those geometric forms only two of the three (triangle) or four (tetrahedron) spin constraints for antiparallel spin alignment can be satisfied at the same time, that is, the system is geometrically frustrated^{5,29} (Figure 10). Keeping in mind, that the magnetic sublattice in $Ce_4O_4Se[Se_2]$ and $Nd_4O_4Se[Se_2]$ is based on a tetrahedral arrangement of rare-earth

metal cations, the magnetic frustration in those compounds arises most likely from the special geometric arrangement of the M^{3+} cations ($M = Ce, Nd$) within the crystal structure, as observed in many other rare-earth metal compounds, which are geometrically frustrated magnetic materials as well, for example pyrochlores $M_2Mn_2O_7$ ($M = Y, Ho$ and Yb)³⁰ and chalcogenide spinels CdM_2S_4 ($M = Ho, Er, Tm, Yb$) and CdM_2Se_4 ($M = Dy, Ho$).³¹

Conclusions

The five oxide selenides $La_4O_4Se[Se_2]$, $Ce_4O_4Se[Se_2]$, $Pr_4O_4Se[Se_2]$, $Nd_4O_4Se[Se_2]$, and $Sm_4O_4Se[Se_2]$ have been synthesized, and the relationship between crystal structure and some physical properties has been studied. These compounds are a good example of how structural building blocks govern physical behavior. The two prominent structural features in the crystal structures of $M_4O_4Se[Se_2]$ ($M = La, Ce, Pr, Nd, Sm$) are diselenide units $[Se_2]^{2-}$ and $[OM_4]^{10+}$ tetrahedra. While the stretching vibration of the diselenide dumbbells involve strong Raman active modes, the $[OM_4]^{10+}$ tetrahedra are responsible for magnetic frustration. Furthermore, the presence of diselenide anions makes those compounds unique in the oxide chalcogenide family. Initial investigations of optical properties indicate that $M_4O_4Se[Se_2]$ ($M = La, Ce, Pr, Nd, Sm$) are semiconducting materials.

Acknowledgment. This work was financially supported by the National Science Foundation, NSF-DMR-0343412 (U.S.A.), the State of Baden-Wuerttemberg (Stuttgart/Germany), the Deutsche Forschungsgemeinschaft (DFG, Bonn/Germany), and the Fonds der Chemischen Industrie (Frankfurt a. M./Germany).

Supporting Information Available: Crystallographic information files (CIF), of $M_4O_4Se[Se_2]$ ($M = La, Ce, Pr, Nd, Sm$) and a detailed description for the calculation of the degree of distortion, $\Delta(\text{dis})$, of the tetrahedral $[OM_4]^{10+}$ building blocks (PDF). This material is available free of charge via the Internet at <http://pubs.acs.org>.

IC800233C

(28) Schiffer, P.; Ramirez, A. P. *Commun. Condens. Matter Phys.* **1996**, *10*, 21–26.

(29) Toulouse, G. *Commun. Phys.* **1977**, *2*, 115–119; Vannimenus, J.; Toulouse, G. *J. Phys. C: Solid State Phys.* **1977**, *10*, L537–L542.

(30) Greedan, J. E.; Raju, N. P.; Maignan, A.; Simon, Ch.; Pedersen, J. S.; Niraimathi, A. M.; Gmelin, E.; Subramanian, M. A. *Phys. Rev. B* **1996**, *54*, 7189–7200.

(31) Lau, G. C.; Freitas, R. S.; Ueland, B. G.; Schiffer, P.; Cava, R. J. *Phys. Rev. B* **2005**, *72*, 054411–054415.